

Article

Optimal Design of a Dual-Pressure Steam Turbine for Rankine Cycle Based on Constructal Theory

Huijun Feng^{1,2,3,4}, Lingen Chen^{1,3,4,*} , Wei Tang² and Yanlin Ge^{1,3,4}

¹ Institute of Thermal Science and Power Engineering, Wuhan Institute of Technology, Wuhan 430205, China; huijunfeng@139.com (H.F.); geyali9@hotmail.com (Y.G.)

² College of Power Engineering, Naval University of Engineering, Wuhan 430033, China; 18202463039@163.com

³ Hubei Provincial Engineering Technology Research Center of Green Chemical Equipment, Wuhan 430205, China

⁴ School of Mechanical & Electrical Engineering, Wuhan Institute of Technology, Wuhan 430205, China

* Correspondence: lingchen@hotmail.com

Abstract: A one-dimensional dual-pressure steam turbine (ST) model for the marine Rankine cycle is built in this paper. Based on constructal theory, the optimal design of the dual-pressure ST is performed with a fixed total volume of the high- and low-pressure STs. The total power output (PO) of the dual-pressure ST is maximized. Seventeen parameters, including the dimensionless average diameters (DADs) of the stages, steam inlet angles (SIAs) of the stages, average reaction degrees (ARDs) of the stages, and volume ratio of the high-pressure ST are taken as optimization variables. The optimal structure parameters of the stages are gained. It reveals that the total PO of the dual-pressure ST is increased by 2.59% by optimizing the average diameter of the Curtis stage, and the change in the total PO is not obvious by optimizing the average diameter of the third stage of the low-pressure ST. Both the total PO and the corresponding efficiency of the dual-pressure ST are increased by 10.8% after simultaneously optimizing 17 variables with the help of the Matlab optimization toolbox. The novelty of this paper is introducing constructal theory into turbine performance optimization by varying seventeen structure, thermal and flow parameters, and the result shows that the constructal optimization effect is remarkable. Optimal designs of practical STs can be guided by the optimization results gained in this paper.

Keywords: constructal theory; steam Rankine cycle; dual-pressure steam turbine; power output; thermal efficiency; optimal structure design



Citation: Feng, H.; Chen, L.; Tang, W.; Ge, Y. Optimal Design of a Dual-Pressure Steam Turbine for Rankine Cycle Based on Constructal Theory. *Energies* **2022**, *15*, 4854. <https://doi.org/10.3390/en15134854>

Academic Editors: Mirko Morini, Dionysia (Denia) Kolokotsa, Yukun Hu, Erik Dahlquist and Esko Juuso

Received: 29 May 2022

Accepted: 28 June 2022

Published: 1 July 2022

Publisher's Note: MDPI stays neutral with regard to jurisdictional claims in published maps and institutional affiliations.



Copyright: © 2022 by the authors. Licensee MDPI, Basel, Switzerland. This article is an open access article distributed under the terms and conditions of the Creative Commons Attribution (CC BY) license (<https://creativecommons.org/licenses/by/4.0/>).

1. Introduction

The steam turbine (ST) [1,2] is an important component for the energy conversion process of a steam Rankine cycle, which converts the thermal energy of the steam into kinetic energy and mechanical energy in turn. There are many parameters for a complex multistage ST, and parameter optimization is one effective way to elevate the performance of the ST.

Many scholars have conducted various performance optimizations for STs. Chen et al. [3] performed multi-optimization of a marine ST stage and analyzed the effect of stage number on the ST efficiency. Qin et al. [4] maximized the stage efficiency of an axial flow ST by varying the geometric and steam flow parameters of the flow passage section and elevated the stage efficiency by up to 1.8%. Ni et al. [5] built a segmented lumped parameter model for a dual-pressure ST (DPST) and compared the simulation and measured results to validate its correctness. Abadi et al. [6] built a turbine blade cascade model with two-phase flows and augmented its efficiency by up to 2.1% after optimization. Anđelić et al. [7] analyzed the performance of a marine ST under different loads and found that the losses and efficiency of the ST augmented with the augment of the turbine load. Zhao et al. [8] considered the guide ring in a low-pressure 300MW ST model and pointed out that the

eddy current was abated, and the efficiency of the low-pressure cylinder was augmented by introducing the guide ring. Vedran et al. [9] calculated the energy efficiency of a three-cylinder ST and pointed out that the energy efficiencies of the three cylinders were 95.08%, 95.02% and 94.92% sorted by the reduction of the cylinder pressure. Moreover, the performance of turbines with organic working fluids has also been investigated by some scholars [10–13].

In the engineering field, constructal theory [14–26] provides a new idea for the optimal design of various transfer systems. For power plants, this theory has been used in the structure optimizations of boilers [27–31], evaporators [32–35], condensers [36–39], regenerators [40,41], turbines [42–47] and whole systems [48–50]. In the constructal research of the turbines, Kim et al. [42] studied the weight distribution problem of a DPST for land power plants with a fixed total weight and gained the maximum power output (PO) and optimal weight distribution. Beyene and Peffley [43] applied constructal theory to the design of a low-speed wind turbine and gained an optimal trailing edge angle, leading to maximizing the PO of the turbine. Feng et al. [44] sought the minimum thermal resistance of a gas turbine blade and reported that a multi-scale structure exhibited good thermal performance. Stanescu et al. [45] built a constructal cooling model for a gas turbine and compared the turbine performances of fog cooling and inter-stage water spraying cooling by numerical calculations. Wu et al. [46] performed a structure design for an ammonia radial turbine and augmented its PO by 2.02% after optimization. Chen et al. [47] built an R245fa axial flow turbine model and sought the optimal volume and inlet pressure of the turbine to elevate its PO.

The essence of constructal theory is constructal law, which can be described as follows: “For a finite-size flow system to persist in time (to live), its configuration must change in time such that it provides easier and easier access to its currents” [14,15]. Structure optimization based on constructal law is called constructal optimization. Different from land turbines, both PO and finite volume should be considered in the design of marine turbines. For this paper, according to the constructal law, in the condition of the fixed total volume (finite size) of the DPST, structure optimization of the ST will be conducted with multi-variable optimization. The PO of the DPST will be maximized. The optimal design variables will be obtained. From this point of view, this paper belongs to constructal design work. In addition, Bejan and colleagues performed similar work [42]. This work is inspired by [42].

This is the biggest difference between this paper and the existing literature. The marine turbine is always composed of two STs with different pressures, and it is important to elevate turbine performance by optimizing its structure under finite size. Based on Refs. [46,47], a one-dimensional DPST model for the marine steam Rankine cycle will be built in this paper. Based on constructal theory, with a fixed total volume of the high- and low-pressure STs, the optimal design of the DPST will be conducted by varying the structure parameters of the stages to search for the maximum PO. The optimization results of the DPST gained by single- and multiple-variable optimizations will be compared. The first novelty of this paper is the introduction of constructal theory into turbine performance optimization. Another novelty of this paper is optimizing the multistage DPST by simultaneously varying seventeen structure, thermal and flow parameters. The performance of the multistage DPST is hoped to be improved by applying these methods.

2. Marine DPST Model

Figure 1 shows a schematic diagram of a marine one-dimensional DPST. The ST is composed of high- and low-pressure axial flow STs in series. The superheated steam generated by a boiler successively enters the high- and low-pressure STs to do work, and finally, the torque generated by the STs is transmitted to the propeller through the reduction gear and shaft. The high-pressure ST is an impulse internal bypass composed of a Curtis stage and nine single-stage STs [5]. The design point condition of the STs is considered in this paper, and only the Curtis stage and the last three single stages are working at this

condition. The low-pressure ST is an impulse double-path one, which is composed of five impulse stages in each path [5]. The low-pressure ST is symmetrical, and exhaust steam is discharged into the condenser from its middle. It is assumed that the stable flow in the ST is insulated from the environment and that the parameters of the steam are only changed along the axis. Thus, the steam in the ST can be viewed as a one-dimensional steady adiabatic flow.

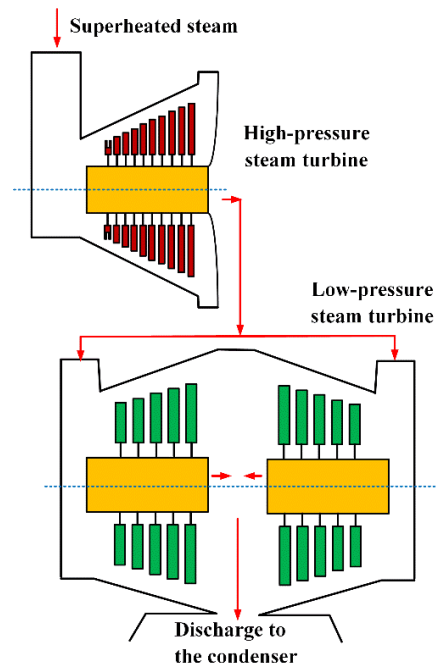


Figure 1. Schematic diagram of a marine DPST model.

2.1. ST Model with Axial Flow

The stage is the smallest unit for the axial flow ST to work. Figure 2 shows the thermodynamic process diagram of a single stage.

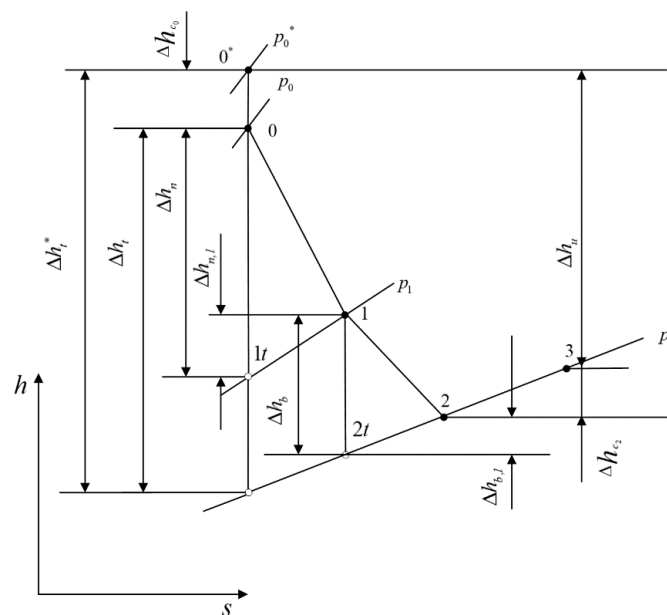


Figure 2. Thermodynamic process diagram of a single stage.

Points 0 (pressure p_0) and 0* (pressure p_{0^*}) are the state points of the steam at the normal and stagnation states in front of the nozzle, respectively. Points 1 (pressure p_1)

and 2 (pressure p_2) are the state points of the steam at the inlet and outlet of the rotating blade. The ideal stagnation enthalpy drop of the steam in the whole stage and ideal enthalpy drops of the steam in the nozzle and rotating blade are Δh_t^* , Δh_n and Δh_b , respectively.

The average reaction degree (ARD, Ω_m) of the single stage is the ratio of the ideal enthalpy drop (Δh_b) in the rotating blade to the ideal stagnation enthalpy drop (Δh_t^*) in the whole stage, i.e.,

$$\Omega_m = \frac{\Delta h_b}{\Delta h_t^*} = \frac{\Delta h_b}{\Delta h_n^* + \Delta h_b} \tag{1}$$

where Δh_n^* is the ideal stagnation enthalpy drop of the steam in the nozzle.

Figure 3 further shows the thermodynamic process diagram of a Curtis stage with a certain reaction degree. Each thermodynamic process of the Curtis stage is similar to that of the single stage, which is not repeated here.

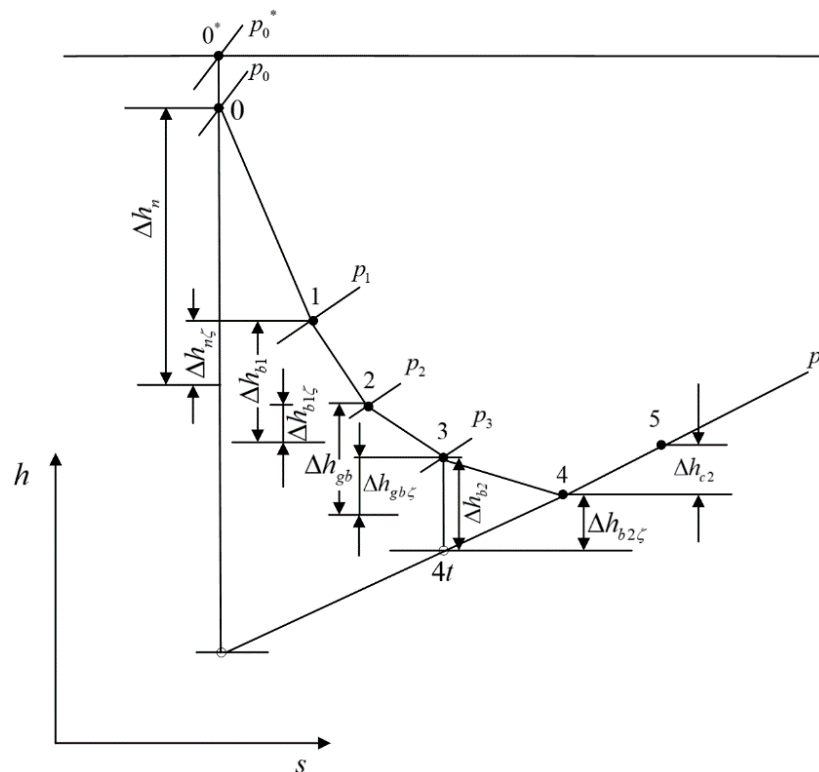


Figure 3. Thermodynamic process diagram of the Curtis stage.

2.1.1. Expansion Process of the Steam in the Nozzle

The ideal velocity (c_{1t}) of the steam flow at the nozzle outlet is

$$c_{1t} = \sqrt{2\Delta h_n^*} \tag{2}$$

when the steam flows through the nozzle, its actual outlet speed (c_1) is less than the ideal speed (c_{1t}) due to the friction and vortex in the nozzle, i.e.,

$$c_1 = \varphi c_{1t} \tag{3}$$

where φ is the nozzle velocity coefficient, whose variation range is from 0.92 to 0.98.

The energy loss ($\Delta h_{n,l}$) of the nozzle with the actual flow is equal to the kinetic energy at the nozzle outlet under the ideal condition minus that under the actual condition, i.e.,

$$\Delta h_{n,l} = \frac{1}{2}(c_{1t}^2 - c_1^2) = \frac{1}{2}c_{1t}^2(1 - \varphi^2) = (1 - \varphi^2)\Delta h_n^* \tag{4}$$

2.1.2. Flow and Energy Conversion Processes of the Steam in a Rotating Cascade

The circumferential velocity (u) at the average diameter (D_b) of the rotating cascade is

$$u = \frac{\pi D_b n}{60} \tag{5}$$

where n is the rotational speed of the ST.

Figure 4 shows the velocity triangle of the single stage. The relative velocity (w_1) and relative inlet angle (β_1) of the steam flow at the inlet of the rotating blade can be calculated according to the velocity triangle.

$$w_1 = \sqrt{c_1^2 + u^2 - 2uc_1 \cos \alpha_1} \tag{6}$$

$$\beta_1 = \arcsin \frac{c_1 \sin \alpha_1}{w_1} = \arctan \frac{c_1 \sin \alpha_1}{c_1 \cos \alpha_1 - u} \tag{7}$$

where α_1 is the absolute angle of the steam flow at the inlet of the rotating blade.

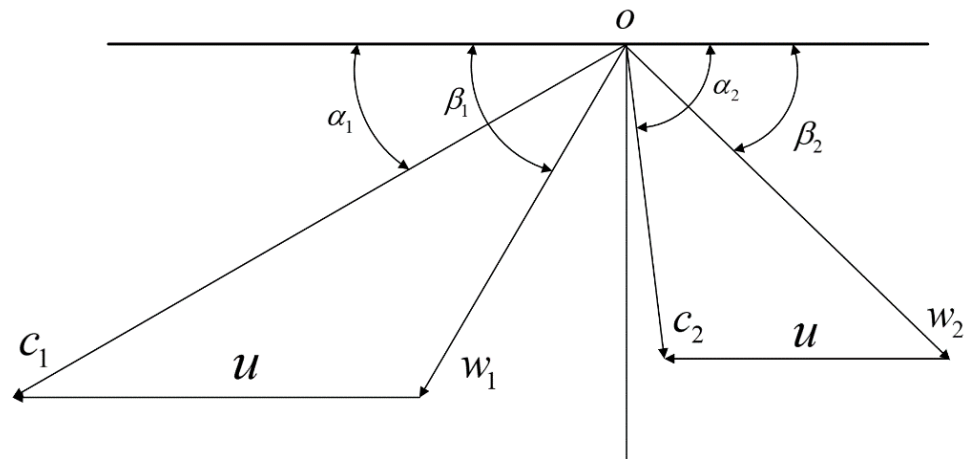


Figure 4. Velocity triangle of a stage.

According to the energy balance equations of the inlet and outlet of the rotating blade, the ideal relative velocity (w_{2t}) of the steam flow at the outlet of the rotating blade can be calculated as

$$w_{2t} = \sqrt{2(h_1 - h_{2t}) + w_1^2} \tag{8}$$

where $h_1 - h_{2t}$ is the ideal enthalpy drop (Δh_b) of the rotating blade. Substituting $\Delta h_b = \Omega_m \Delta h_t^*$ into Equation (8), one has

$$w_{2t} = \sqrt{2\Omega_m h_t^* + w_1^2} = \sqrt{2h_b^*} \tag{9}$$

where $\Delta h_b^* (= \Delta h_b + 0.5w_1^2)$ is the ideal stagnation enthalpy drop of the rotating blade.

The absolute velocity (c_2) and absolute angle (α_2) of the steam flow at the outlet of the rotating blade can be given as

$$c_2 = \sqrt{w_2^2 + u^2 - 2uw_2 \cos \beta_2} \tag{10}$$

$$\alpha_2 = \arctan \frac{w_2 \sin \beta_2}{w_2 \cos \beta_2 - u} \tag{11}$$

where w_2 and β_2 are the ideal relative velocity and relative angle of the steam flow at the outlet of the rotating blade, respectively.

Similarly, energy loss exists when steam goes through the rotating cascade. The actual relative velocity (w_2) at the rotating blade outlet is less than the ideal relative velocity, i.e.,

$$w_2 = \psi w_{2t} = \psi \sqrt{2h_b^*} \tag{12}$$

where ψ is the speed coefficient of the rotating blade, whose variation range is from 0.85 to 0.95.

The energy loss ($\Delta h_{b,l}$) of the steam going through the rotating blade, named the rotating blade loss, can be expressed as

$$\Delta h_{b,l} = (w_{2t}^2 - w_2^2) / 2 = (1 - \psi^2) \Delta h_b^* \tag{13}$$

The residual speed loss (Δh_{c2}) of the steam flow caused by the kinetic energy of the exhaust steam is

$$\Delta h_{c2} = c_2^2 / 2 \tag{14}$$

where c_2 is the absolute speed at the outlet of the rotating blade.

In the multistage ST, the kinetic energy carried by the residual speed can be used by the next stage, and its degree of utilization can be expressed by the utilization coefficient μ ($0 \leq \mu \leq 1$) of the residual speed.

After considering the energy losses of the nozzle, rotating blade and residual speed, the effective specific enthalpy (Δh_u) of a turbine stage is expressed as

$$\Delta h_u = \mu_0 c_0^2 / 2 + \Delta h_n + \Delta h_b - (\Delta h_{n,l} + \Delta h_{b,l} + \Delta h_{c2}) \tag{15}$$

where μ_0 is the utilization coefficient of the residual speed.

Figure 5 further shows the velocity triangle of the Curtis stage, and its velocity relationship is similar to Figure 4, which is not repeated here.

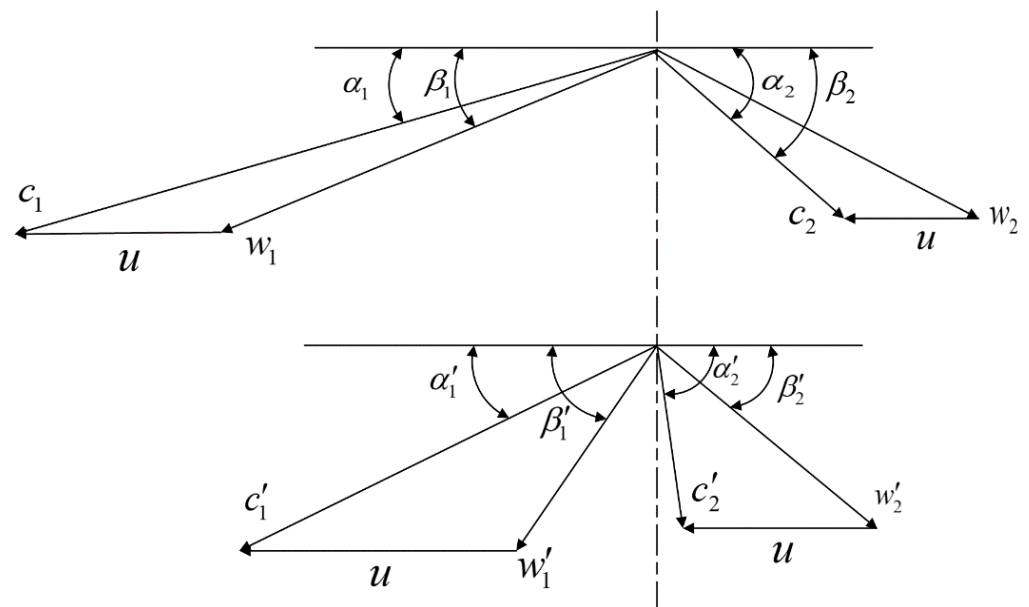


Figure 5. Velocity triangle of a Curtis stage.

2.1.3. Loss Model in the Stage

In addition to nozzle loss, rotating blade loss and residual speed loss, there exist other losses in the stage, such as spanwise loss, sector loss, impeller friction loss, partial inlet steam loss, steam leakage loss and wet steam loss.

(1) Spanwise loss (Δh_l)

The spanwise loss is the additional loss along the height of the blade, which is often calculated by the semi-empirical formula [51], i.e.,

$$\Delta h_l = \frac{a}{l} \Delta h_u \quad (16)$$

where the empirical coefficient a is usually 1.2 for the single stage and 2.0 for the Curtis stage; the cascade height l is the nozzle height for the single stage and the average height of the cascades for the Curtis stage; Δh_u is the effective specific enthalpy drop of the stage.

(2) Sector loss (Δh_θ)

Sector loss is the additional loss caused by the deviation from the design condition, which is often calculated by the semi-empirical formula [51], i.e.,

$$\Delta h_\theta = E_0 \zeta_\theta \quad (17)$$

$$\zeta_\theta = 0.7 \left(\frac{l_b}{D_b} \right)^2 \quad (18)$$

where l_b is the height of the rotating blade, and E_0 is the ideal energy of the stage.

(3) Impeller friction loss (Δh_f)

The impeller friction loss is the additional loss caused by the friction movement between the impeller surface and steam, which is often calculated by the semi-empirical formula [51], i.e.,

$$\Delta h_f = \frac{3600 \Delta p_f}{\dot{m}_{st}} \quad (19)$$

$$\Delta p_f = k_1 \left(\frac{u}{100} \right)^3 D_m^2 \frac{1}{v} \quad (20)$$

where Δp_f is the friction power consumption of the impeller, \dot{m}_{st} is the steam mass flow rate of the stage, k_1 is the empirical coefficient, D_m is the average diameter of the stage, and v is the average specific volume of the steam.

(4) Admission loss (Δh_e)

The admission loss is composed of the blast loss (Δh_w) and steam rejection loss (Δh_s). Δh_w can be calculated as [51]:

$$\Delta h_w = B_e \frac{1}{e} (1 - e - 0.5e_c) E_0 x_a^3 \quad (21)$$

where e_c is the ratio of the arc length of the protective cover to the whole circumference length; e is the admission degree; and the stage type coefficient (B_e) of the ST is set as 0.15 for the single stage and 0.55 for the Curtis stage. Δh_s can be calculated as [51]:

$$\Delta h_s = c_s \frac{1}{e} \frac{Z_n}{D_n} E_0 x_a \quad (22)$$

where Z_n is the group number of the nozzles; D_n is the average diameter of the stationary cascade; and the coefficient (c_s) related to the stage type of the ST is set as 0.012 for the single stage and 0.016 for the Curtis stage.

Therefore, the total admission loss in this stage is:

$$\Delta h_e = \Delta h_w + \Delta h_s \quad (23)$$

(5) Steam leakage loss (Δh_δ)

The steam leakage loss is composed of the partition leakage loss (Δh_p) and blade top leakage loss (Δh_t). The leakage mass flow rate (Δm_p) of the steam from the partition is given as [51]:

$$\Delta m_p = \mu_p A_p \frac{\sqrt{2\Delta h_n^*}}{v_{1t} \sqrt{z_p}} \quad (24)$$

where μ_p is the discharge coefficient of the steam seal, A_p is the clearance area of the steam seal, v_{1t} is the ideal specific volume of the steam at the outlet of the steam seal teeth, and z_p is the teeth number of the steam seal.

Δh_p can be calculated as [51]:

$$\Delta h_p = \frac{\Delta m_p}{m_{st}} \Delta h_u \quad (25)$$

The leakage mass flow rate (Δm_t) of the blade top is given as [51]:

$$\Delta m_t = \frac{e\mu_t \pi (D_b + l_b) \bar{\delta}_t \sqrt{2\Omega_t \Delta h_t^*}}{v_{2t}} \quad (26)$$

where μ_t is the discharge coefficient of the blade top clearance, μ_n is the discharge coefficient of the nozzle, Ω_t is the reaction degree of the blade top, and $\bar{\delta}_t$ is the equivalent clearance of the blade top for steam leakage.

Δh_t can be calculated as [51]:

$$\Delta h_t = \frac{\Delta m_t}{m_t} \Delta h_u \quad (27)$$

Therefore, the total steam leakage loss (Δh_δ) in the stage is:

$$\Delta h_\delta = \Delta h_p + \Delta h_t \quad (28)$$

(6) Wet steam loss (Δh_x)

When the steam flows into the last few stages of the turbine, a wet steam area is generated. The wet steam loss is usually calculated using the following empirical formula [51]:

$$\Delta h_x = (1 - x_m) \Delta h_u \quad (29)$$

where x_m is the average steam dryness.

2.1.4. Internal Power of the Stage

According to the internal losses of the stage, the effective enthalpy drop (Δh_i) of the stage can be given as

$$\Delta h_i = \Delta h_u - (\Delta h_l + \Delta h_\theta + \Delta h_f + \Delta h_e + \Delta h_\delta + \Delta h_x) \quad (30)$$

The calculation process of the internal power of the stage is shown in Figure 6. Finally, the internal power (P_i) of a stage is given as

$$P_i = \dot{m}_{st} \Delta h_i \quad (31)$$

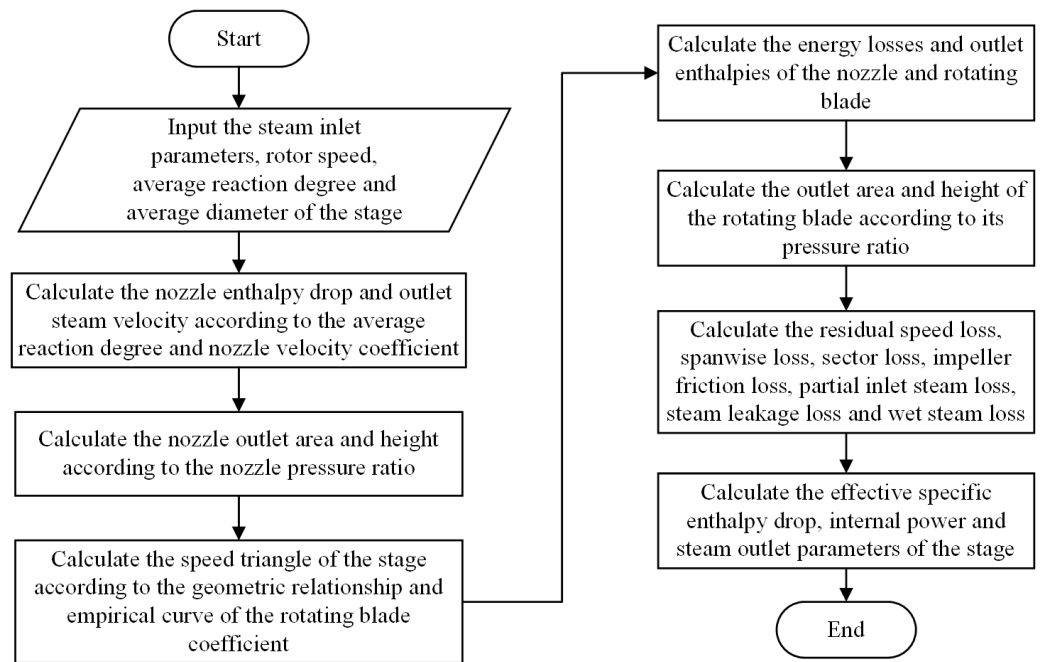


Figure 6. Calculation process of the internal power and steam outlet parameters of the stage.

To illustrate the ST model more intuitively, the loss models and internal power of the stage are further listed in Table 1.

Table 1. Lists of the loss models and the internal power of the stage.

Items	Expressions	Equation Numbers
Nozzle energy loss	$\Delta h_{n,l} = \frac{1}{2}(c_{1t}^2 - c_1^2) = \frac{1}{2}c_{1t}^2(1 - \varphi^2) = (1 - \varphi^2)\Delta h_n^*$	Equation (4)
Rotating blade loss	$\Delta h_{b,l} = \frac{1}{2}(w_{2t}^2 - w_2^2) = (1 - \psi^2)\Delta h_b^*$	Equation (13)
Residual speed loss	$\Delta h_{c2} = \frac{1}{2}c_2^2$	Equation (14)
Spanwise loss	$\Delta h_l = \frac{q}{l}\Delta h_u$	Equation (16)
Sector loss	$\Delta h_\theta = E_0\zeta_\theta$	Equation (17)
Impeller friction loss	$\Delta h_f = \frac{3600\Delta p_f}{\dot{m}_{st}}$	Equation (19)
Admission loss	$\Delta h_e = B_e \frac{1}{e}(1 - e - 0.5e_c)E_0x_a^3 + c_s \frac{1}{e} \frac{Z_u}{D_n} E_0x_a$	Equation (23)
Steam leakage loss	$\Delta h_\delta = \frac{\Delta m_p}{\dot{m}_{st}}\Delta h_u + \frac{\Delta m_t}{\dot{m}_t}\Delta h_u$	Equation (25)
Wet steam loss	$\Delta h_x = (1 - x_m)\Delta h_u$	Equation (29)
Effective enthalpy drop of the stage	$\Delta h_i = \Delta h_u - (\Delta h_l + \Delta h_\theta + \Delta h_f + \Delta h_e + \Delta h_\delta + \Delta h_x)$	Equation (30)
Internal power (P_i) of the stage	$P_i = \dot{m}_{st}\Delta h_i$	Equation (31)

2.1.5. Volume of the DPST

The average stage diameters ($D_{m,j}$, $j = H, L$) of the high- and low-pressure STs are calculated as

$$D_{m,j} = \frac{D_{1,j} + D_{z,j}}{2} \quad (j = H, L) \tag{32}$$

where $D_{1,j}$ and $D_{z,j}$ are the average diameters of the first and last stages, respectively. For simplification, the average diameters of the stationary cascade and rotating cascade are approximately equal to those of the stage.

The average diameters ($D_{a,j}$, $j = H, L$) of the turbine casing and maximum lengths ($L_{a,j}$, $j = H, L$) of the high- and low-pressure STs can be approximately gained based on the empirical coefficients.

$$D_{a,j} = \beta_j \cdot D_{m,j} \quad (j = H, L) \tag{33}$$

$$L_{a,j} = \alpha_j \cdot L_{sp,j} \quad (j = H, L) \tag{34}$$

where $L_{sp, j}$ is the flow passage length of the ST, and β_j and α_j are the coefficients of the average diameter and length, respectively.

The volumes (V_{HT} and V_{LT}) of the high- and low-pressure STs can be approximately calculated as

$$V_{HT} = \frac{\pi(D_{a, H})^2}{4} \cdot L_{a, H} \tag{35}$$

$$V_{LT} = \frac{\pi(D_{a, L})^2}{4} \cdot L_{a, L} \tag{36}$$

The total volume (V_T) of the DPST is

$$V_T = V_{HT} + V_{LT} \tag{37}$$

2.2. Performance of the DPST

The new steam generated by the boiler enters the high- and low-pressure STs to do the work. Under the design point working condition, the steam only goes through the Curtis stage and last three single stages in the high-pressure ST. Therefore, the PO ($P_{T, H}$) of the high-pressure ST is the sum of the POs of these four stages.

$$P_{T, H} = P_{i, DSH} + P_{i, H1} + P_{i, H2} + P_{i, H3} \tag{38}$$

The low-pressure ST is symmetric. Therefore, the PO ($P_{T, L}$) of the low-pressure ST is the sum of the POs of all symmetric stages.

$$P_{T, L} = 2(P_{i, L1} + P_{i, L2} + P_{i, L3} + P_{i, L4} + P_{i, L5}) \tag{39}$$

The calculation process of the PO of the DPST is shown in Figure 7. The total PO (P_t) of the multistage ST is the sum of the POs of the high- and low-pressure STs.

$$P_t = P_{T, H} + P_{T, L} \tag{40}$$

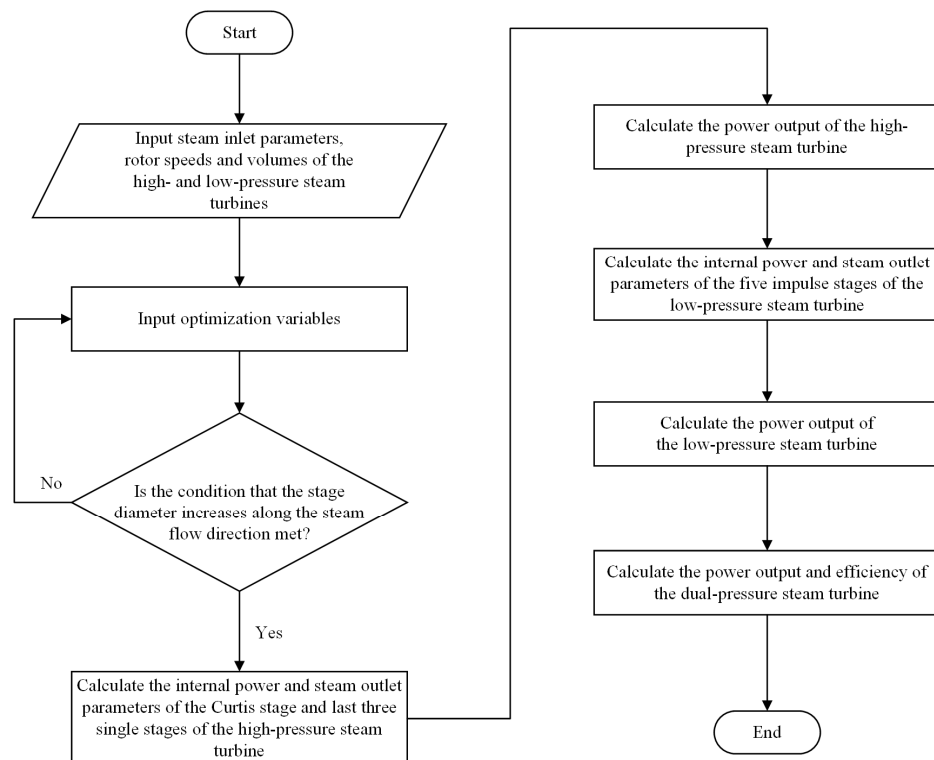


Figure 7. Calculation process of the power output and efficiency of the DPST.

The theoretical PO (P_{the}) of the ST is defined as the energy released by the steam.

$$P_{\text{the}} = \dot{m}_{\text{st}}(h_0^* - h_{\text{out}, L5}) \quad (41)$$

where h_0^* and $h_{\text{out}, L5}$ are the steam stagnation enthalpy at the inlet of the high-pressure ST and steam enthalpy at the outlet of the low-pressure ST, respectively.

The thermal efficiency (η_t) of the DPST is defined as the ratio of the total PO to the theoretical PO.

$$\eta_t = \frac{P_t}{P_{\text{the}}} \quad (42)$$

3. Optimal Design of the DPST Based on Constructal Theory

In this section, with a fixed total volume of the DPST, the constructal design of the double-pressure ST will be conducted subjected to the geometric constraints of increasing dimensionless average diameters (DADs) of the stages along the direction of steam flow. The dimensionless average diameter is defined as the ratio of the current value of the average diameter to its initial value. The effects of the DADs and steam inlet angle (SIA) of the stages on the total PO of the DPST will be analyzed first, and the results can guide the following multivariable optimization. To illustrate the multi-variable optimization problem more intuitively, the constant parameters, design variables, optimization objective, and constraints of the model are listed in Table 2. Then, the total PO will be optimized by simultaneously varying the design variables in Table 2. Due to the parameter settings and geometric constraints of the DPST, the available variation range of one parameter will be different in the following figures. Moreover, the difference between the theoretical and actual total POs of the DPST under the initial parameters is 0.3%, which validates the correctness of the theoretical model.

Table 2. Constant parameters, design variables, optimization objective, and constraints of the model.

Items	Contents
Constant parameters	Steam mass flow rate (\dot{m}_{st}), pressure (p_0), temperature (T_0), total volume (V_T) and rotational speed (n)
Design variables	DADs ($\tilde{D}_{m, \text{DSH}}$, $\tilde{D}_{m, \text{H1}}$, $\tilde{D}_{m, \text{H3}}$, $\tilde{D}_{m, \text{L1}}$, $\tilde{D}_{m, \text{L3}}$, $\tilde{D}_{m, \text{L4}}$ and $\tilde{D}_{m, \text{L5}}$), SIAs ($\alpha_{1, \text{DSH}}$, $\alpha_{3, \text{DSH}}$, α_{H1} and α_{L1}), ARDs (Ω_{b1} , Ω_{gb} , Ω_{b2} , Ω_{H} and Ω_{L}) and volume ratio (x_v)
Optimization objective	Total PO (P_t) of the multistage DPST
Constraints	Total volume (V_T) of the DPST and increasing average DADs of the stages along the flow direction

Figure 8 shows the relationship between the dimensionless total PO (\tilde{P}_t) of the DPST and DAD ($\tilde{D}_{m, \text{DSH}}$) of the Curtis stage of the high-pressure ST. Figure 8 shows that when the SIA ($\alpha_{1, \text{DSH}}$) of the first row of the rotating blade is 14° , with the augment of $\tilde{D}_{m, \text{DSH}}$, \tilde{P}_t first abates and then augments. This is because when $\tilde{D}_{m, \text{DSH}}$ changes from 0.820 to 0.831, the PO of the high-pressure ST continuously abates, and its decrement is bigger than the PO increment of the low-pressure ST. Finally, the total PO of the ST shows an abating trend. When $\tilde{D}_{m, \text{DSH}}$ changes from 0.831 to 0.845, the POs of the high- and low-pressure STs augment, so the total PO shows an augmenting trend. When $\alpha_{1, \text{DSH}} = 14^\circ$, within the discussed variation range of $\tilde{D}_{m, \text{DSH}}$ determined by the geometric constraints of the stages, \tilde{P}_t reaches the maximum ($\tilde{P}_{t, \text{max}}$) at 1.0259, and the corresponding optimal DAD ($\tilde{D}_{m, \text{DSH}, \text{opt}}$) is 0.845. The total PO of the DPST is augmented by 2.59% after optimization. In addition, for a fixed $\tilde{D}_{m, \text{DSH}}$, \tilde{P}_t augments with the abatement of $\alpha_{1, \text{DSH}}$.

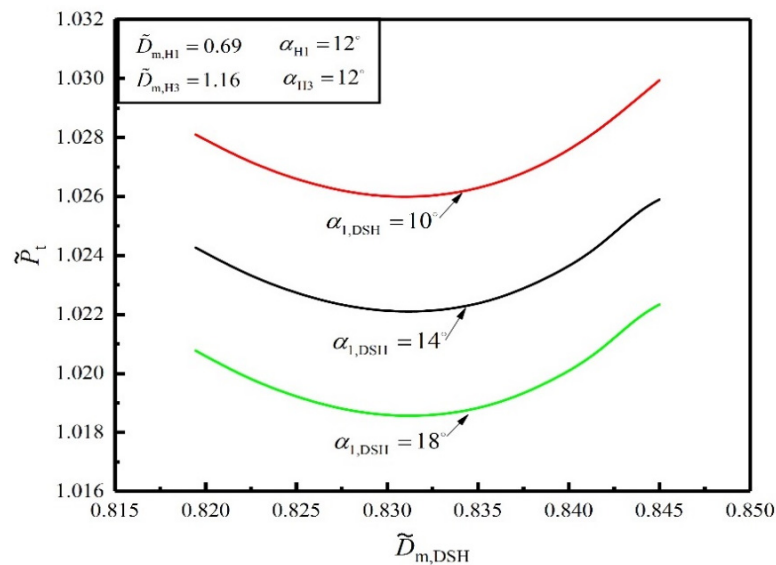


Figure 8. Relationship between \tilde{P}_t and $\tilde{D}_{m, DSH}$ with different $\alpha_{1, DSH}$.

Figure 9 shows the relationship between the dimensionless total PO (\tilde{P}_t) of the DPST and DAD ($\tilde{D}_{m, H1}$) of the third stage from the last of the high-pressure ST. As shown in Figure 9, when the SIA (α_{H1}) of this stage is 12° , with the augment of $\tilde{D}_{m, H1}$, \tilde{P}_t continuously abates. When $\alpha_{H1} = 12^\circ$, within the discussed variation range of $\tilde{D}_{m, H1}$, \tilde{P}_t reaches the maximum ($\tilde{P}_{t, \max}$) at 1.0227, and the optimal DAD ($\tilde{D}_{m, H1, \text{opt}}$) is 0.68. The total PO of the DPST is augmented by 2.27% after optimization. In addition, for a fixed $\tilde{D}_{m, H1}$, \tilde{P}_t augments with the augment of α_{H1} .

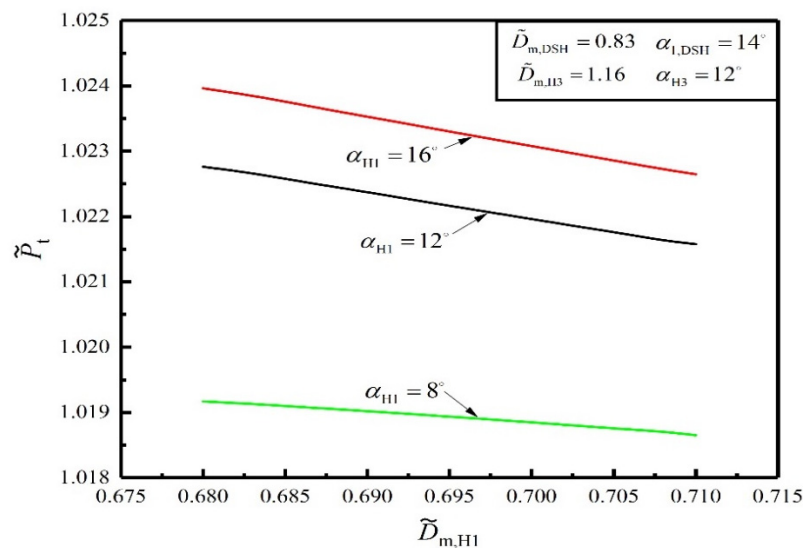


Figure 9. Relationship between \tilde{P}_t and $\tilde{D}_{m, H1}$ with different α_{H1} .

Figure 10 shows the relationship between the dimensionless total PO (\tilde{P}_t) of the DPST and DAD ($\tilde{D}_{m, H3}$) of the last stage of the high-pressure ST. As shown in Figure 10, when the SIA (α_{H3}) of this stage is 12° , with the augment of $\tilde{D}_{m, H3}$, \tilde{P}_t first abates and then augments. When $\alpha_{H3} = 12^\circ$, within the discussed variation range of $\tilde{D}_{m, H3}$, \tilde{P}_t reaches the maximum ($\tilde{P}_{t, \max}$) at 1.0264, and the optimal DAD ($\tilde{D}_{m, H3, \text{opt}}$) is 1.17. The total PO of the DPST is augmented by 2.64% after optimization. In addition, for a fixed $\tilde{D}_{m, H3}$, \tilde{P}_t augments with the augment of α_{H3} , but the increment gradually becomes small.

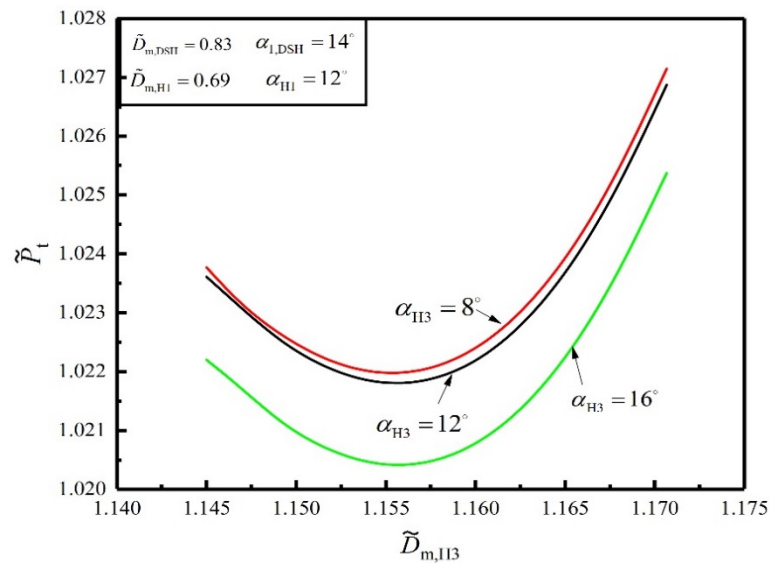


Figure 10. Relationship between \tilde{P}_t and $\tilde{D}_{m, H3}$ with different α_{H3} .

Figure 11 shows the relationship between the dimensionless total PO (\tilde{P}_t) of the DPST and DAD ($\tilde{D}_{m, L1}$) of the first stage of the low-pressure ST. As shown in Figure 11, when the SIA (α_{L1}) of this stage is 23° , with the augment of $\tilde{D}_{m, L1}$, \tilde{P}_t first augments and then abates. When $\alpha_{L1} = 23^\circ$, within the discussed variation range of $\tilde{D}_{m, L1}$, \tilde{P}_t reaches the maximum ($\tilde{P}_{t, max}$) at 1.0016, and the optimal DAD ($\tilde{D}_{m, L1, opt}$) is 0.984. The total PO of the DPST is only augmented by 0.16% after optimization, which shows that the optimization effect is not obvious. Furthermore, for a fixed $\tilde{D}_{m, L1}$, \tilde{P}_t augments with the abatement of α_{L1} .

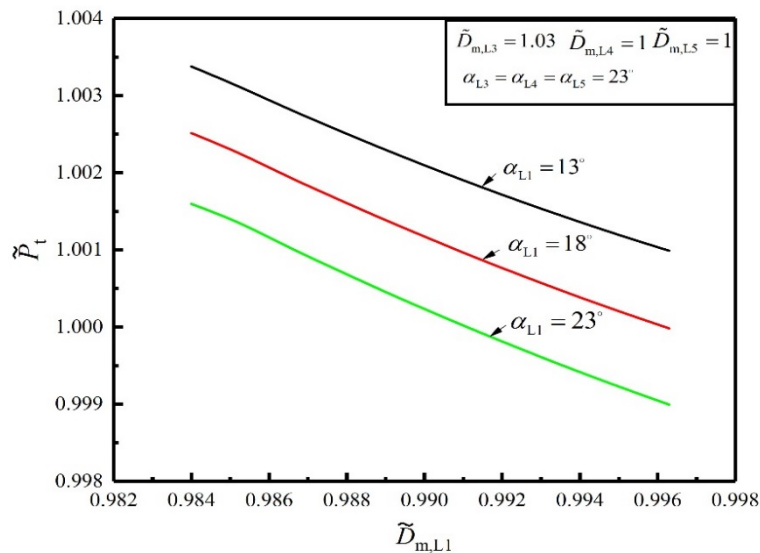


Figure 11. Relationship between \tilde{P}_t and $\tilde{D}_{m, L1}$ with different α_{L1} .

Figure 12 shows the relationship between the dimensionless total PO (\tilde{P}_t) of the DPST and DAD ($\tilde{D}_{m, L4}$) of the fourth stage of the low-pressure ST. As shown in Figure 12, when the SIA (α_{L4}) of this stage is 23° , with the augment of $\tilde{D}_{m, L4}$, \tilde{P}_t continuously augments. When $\alpha_{L4} = 23^\circ$, within the discussed variation range of $\tilde{D}_{m, L4}$, \tilde{P}_t reaches the maximum ($\tilde{P}_{t, max}$) at 1.0007, and the optimal DAD ($\tilde{D}_{m, L4, opt}$) is 1.01. The total PO of the DPST is only augmented by 0.07% after optimization, which shows that the optimization effect is also not obvious. Furthermore, for a fixed $\tilde{D}_{m, L4}$, \tilde{P}_t augments with the abatement of α_{L4} .

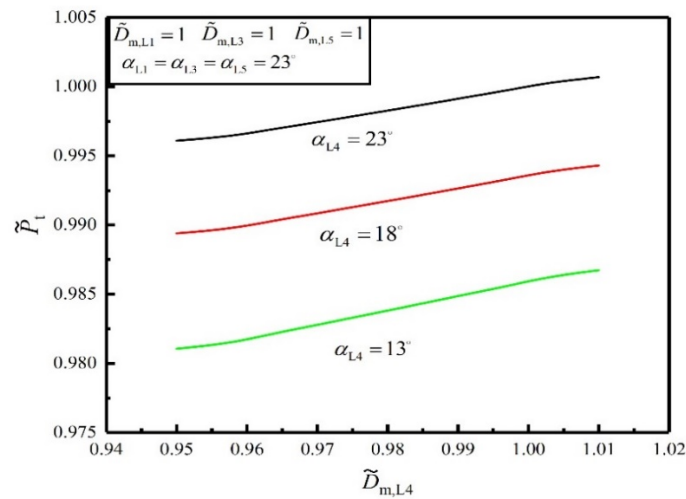


Figure 12. Relationship between \tilde{P}_t and $\tilde{D}_{m, L4}$ with different α_{L4} .

Figure 13 shows the relationship between the dimensionless total PO (\tilde{P}_t) of the DPST and DAD ($\tilde{D}_{m, L5}$) of the fifth stage of the low-pressure ST. Figure 13 shows that when the SIA (α_{L5}) of this stage is 23° , with the augment of $\tilde{D}_{m, L5}$, \tilde{P}_t continuously abates. When $\alpha_{L5} = 23^\circ$, within the discussed variation range of $\tilde{D}_{m, L5}$, \tilde{P}_t reaches the maximum ($\tilde{P}_{t,max}$) at 1.012, and the optimal DAD ($\tilde{D}_{m, L5, opt}$) is 1.16. The total PO of the DPST is only augmented by 1.2% after optimization. Furthermore, for a fixed $\tilde{D}_{m, L5}$, \tilde{P}_t augments with the augment of α_{L5} .

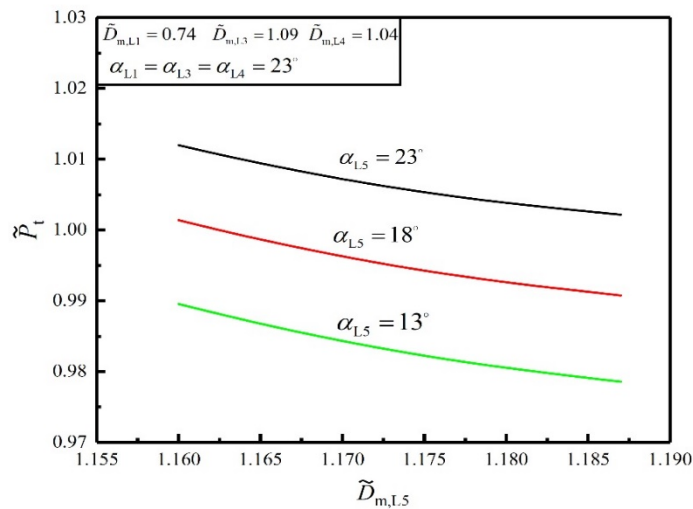


Figure 13. Relationship between \tilde{P}_t and $\tilde{D}_{m, L5}$ with different α_{L5} .

The single variable optimizations of $\tilde{D}_{m, DSH}$, $\tilde{D}_{m, H1}$, $\tilde{D}_{m, H3}$, $\tilde{D}_{m, L1}$, $\tilde{D}_{m, L3}$, $\tilde{D}_{m, L4}$ and $\tilde{D}_{m, L5}$ are conducted in the above discussions. For the DPST, many parameters can be taken as optimization variables. As listed in Table 3, seventeen parameters will be considered in the following constructal optimization with multiple variables to elevate the PO of the DPST. The seventeen parameters include the DADs ($\tilde{D}_{m, DSH}$, $\tilde{D}_{m, H1}$ and $\tilde{D}_{m, H3}$) of the Curtis stage, third stage from last and last stage of the high-pressure ST, the DADs ($\tilde{D}_{m, L1}$, $\tilde{D}_{m, L3}$, $\tilde{D}_{m, L4}$ and $\tilde{D}_{m, L5}$) of the first, third, fourth and fifth stages of the low-pressure ST, SIAs ($\alpha_{1, DSH}$ and $\alpha_{3, DSH}$) of the first and second rows of the rotating blade for the Curtis stage, SIAs (α_{H1} and α_{L1}) of the third stage from last of the high-pressure ST and first stage of the low-pressure ST, ARDs (Ω_{b1} and Ω_{b2}) of the first and second rows of the rotating blade for the Curtis stage, ARD (Ω_{gb}) of the guide vane for the Curtis stage, ARDs (Ω_H and Ω_L) of the single row stages for the high- and low-pressure STs as well as

volume ratio (x_v) of the high-pressure ST. Among these, the form of the DAD for each stage is dimensionless, which is divided by its initial value. The selected optimization variables and their variation ranges are listed in Table 3. The Matlab software function of “fmincon” is applied to search for the maximum total PO, and the “interior-point” algorithm is adopted in this function. Both the total tolerances of the variables and the optimization objective are set as 10^{-20} . The maximum iteration number is set as 200. Figure 14 shows the relationship between \tilde{P}_t and iteration number with different initial values in the function of “fmincon”. This indicates that the optimization results are slightly influenced by the initial values. For this reason and the local optimization solver of the “fmincon” function, different initial variable values are tried to ensure the stability of the optimization results.

Table 3. Optimization variables of constructal design for a DPST.

Number	Variables	Names of the Variables	Variation Ranges
1	\tilde{D}_m, DSH	DAD of the Curtis stage	0.69~1.32
2	$\tilde{D}_m, H1$	DAD of the third stage from last of the high-pressure ST	0.69~1.32
3	$\tilde{D}_m, H3$	DAD of the last stage of the high-pressure ST	0.67~1.27
4	$\tilde{D}_m, L1$	DAD of the first stage of the low-pressure ST	0.86~1.36
5	$\tilde{D}_m, L3$	DAD of the third stage of the low-pressure ST	0.80~1.26
6	$\tilde{D}_m, L4$	DAD of the fourth stage of the low-pressure ST	0.76~1.20
7	$\tilde{D}_m, L5$	DAD of the fifth stage of the low-pressure ST	0.70~1.0
8	α_1, DSH	SIA of the first row of the rotating blade for the Curtis stage	8~25°
9	α_3, DSH	SIA of the second row of the rotating blade for the Curtis stage	8~25°
10	Ω_{b1}	ARD of the first row of the rotating blade for the Curtis stage	0.05~0.2
11	Ω_{gb}	ARD of the guide vane for the Curtis stage	0.05~0.2
12	Ω_{b2}	ARD of the second row of the rotating blade for the Curtis stage	0.05~0.2
13	α_{H1}	SIA of the third stage from last of the high-pressure ST	8~25°
14	α_{L1}	SIA of the first stage of the low-pressure ST	8~25°
15	Ω_H	ARD of the single row stage for the high-pressure ST	0.05~0.2
16	Ω_L	ARD of the single row stage for the low-pressure ST	0.05~0.2
17	x_v	Volume ratio of the high-pressure ST	0.05~0.4

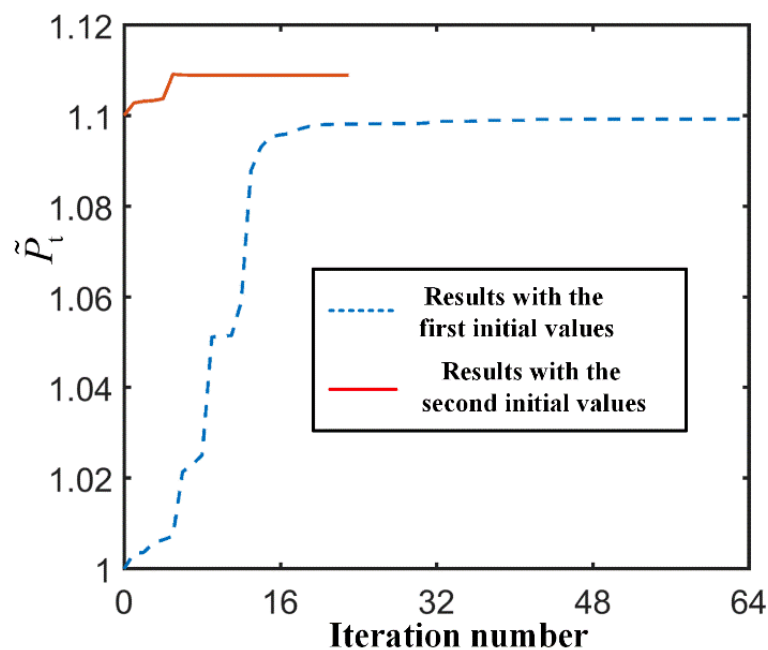


Figure 14. Relationship between \tilde{P}_t and iteration number with different initial values.

After simultaneously optimizing the above seventeen variables, the dimensionless maximum PO and the corresponding results of the DPST are obtained, which are listed in Table 4. In Table 4, after constructal optimization, both the total PO and the corresponding efficiency of the DPST are augmented by 10.8%. This reveals that the structure parameter optimization with multiple variables significantly improves the performance of the DPST compared to that with a single variable.

Table 4. Multiple-variable optimization results of the DPST.

Optimization Objectives and Variables	Before Optimization	After Optimization
\tilde{P}_t	1.0	1.108
η_t	0.875	0.97
$\tilde{D}_{m, DSH}$	1.0	0.69
$\tilde{D}_{m, H1}$	1.0	0.69
$\tilde{D}_{m, H3}$	1.0	0.77
$\tilde{D}_{m, L1}$	1.0	0.86
$\tilde{D}_{m, L3}$	1.0	1.24
$\tilde{D}_{m, L4}$	1.0	1.18
$\tilde{D}_{m, L5}$	1.0	1.1
$\alpha_{1, DSH}$	14°	8°
$\alpha_{3, DSH}$	23.4°	8°
Ω_{b1}	0.12	0.05
Ω_{gb}	0.12	0.05
Ω_{b2}	0.12	0.05
$\alpha_{1, H}$	12°	25°
$\alpha_{1, L}$	23°	25°
Ω_H	0.12	0.2
Ω_L	0.12	0.2
x_v	0.16	0.08

4. Conclusions

A one-dimensional model of a marine dual-pressure axial flow ST is researched in this paper. With fixed total volume of the high- and low-pressure STs, constructal design of the DPST is implemented by altering the DADs, SIAs and ARDs of the stages. The maximum total PO and the corresponding optimal construct of the DPST are gained. The results are summarized as follows:

(1) For the single-variable optimization, within the discussion scopes of the DADs of the stages, the total PO of the DPST is augmented by 2.59% after optimizing the DAD of the Curtis stage, and the change in the total PO is not obvious after optimizing the DAD of the third stage of the low-pressure ST. Within the certain variation ranges, the total PO of the DPST can be further improved by abating the SIA of the first row of the rotating blade for the Curtis stage and SIA of the last stage of the high-pressure ST and augmenting the SIAs of the third, fourth and fifth stages of the low-pressure ST, respectively.

(2) For the multiple-variable optimization, both the total PO and the corresponding efficiency of the DPST are augmented by 10.8% after simultaneously optimizing 17 variables. This reveals that the structure parameter optimization with multiple variables significantly improves the performance of the DPST compared to that with a single variable.

The DPST model with various loss items is considered in this paper. The loss items and volume of the DPST are estimated by the empirical formulas. A more practical model of the DPST will be established in the future, and more practical guidelines will be offered for the optimal designs of axial flow STs to enhance the energy saving and consumption reduction of marine steam power plants.

Author Contributions: Conceptualization, H.F. and L.C.; Data curation, W.T. and Y.G.; Funding acquisition, L.C.; Methodology, H.F., L.C., W.T. and Y.G.; Software, H.F. and W.T.; Supervision, L.C.; Validation, W.T. and Y.G.; Writing—Original draft preparation, H.F. and W.T.; Writing—Reviewing and Editing, L.C. All authors have read and agreed to the published version of the manuscript.

Funding: This paper is supported by the National Natural Science Foundation of China (Grant Nos. 52171317, 51779262, 51979278).

Institutional Review Board Statement: Not applicable.

Informed Consent Statement: Not applicable.

Acknowledgments: The authors wish to thank the reviewers for their careful, unbiased and constructive suggestions, which led to this revised manuscript.

Conflicts of Interest: The authors declare no conflict of interest.

Nomenclature

a	Empirical coefficient
B_e	Stage type coefficient
c	Absolute velocity (m/s)
D_a	Average diameter of the turbine casing (m)
D_b	Average diameter of the rotating cascade (m)
D_m	Average diameter of the stage (m)
D_n	Average diameter of the stationary cascade (m)
e_c	Length ratio
k_1	Empirical coefficient
L_a	Maximum length of the ST (m)
l	Cascade height (m)
l_b	Height of the rotating blade (m)
\dot{m}_{st}	Steam mass flow rate of the stage (kg/s)
n	Rotational speed (Revolutions/s)
P_i	Internal power (kW)
$P_{T,H}$	Power output of the high-pressure ST (kW)
$P_{T,L}$	Power output of the low-pressure ST (kW)
P_t	Total power output of the multistage ST (kW)
P_{the}	Theoretical power output of the ST (kW)
p_0	Pressure (Pa)
u	Circumferential velocity (m/s)
V_{HT}	Volume of the high-pressure ST (m ³)
V_{LT}	Volume of the low-pressure ST (m ³)
V_T	Total volume of the dual-pressure ST (m ³)
v	Average specific volume of the steam (m ⁻³)
w	Relative velocity (m/s)
x_m	Average dryness of the steam
x_v	Volume ratio of the high-pressure ST
Z_n	Group number of the nozzles

Greek symbols

α	Absolute angle (degree)
β	Relative angle (degree)
η_t	Efficiency of the dual-pressure ST
μ	Utilization coefficient
μ_p	Discharge coefficient
φ	Nozzle velocity coefficient
ψ	Speed coefficient
Δh_n	Enthalpy drop (kJ)
Δm_p	Leakage mass flow rate of the steam (m/s)
Δp_f	Friction power consumption of the impeller (kW)
Ω_m	Average reaction degree

Superscript

~	Dimensionless
*	Stagnation state
.	Rate

Subscripts

b	Rotating blade
DSH	Curtis stage of the high-pressure
H	High-pressure
i	Internal
L	Low-pressure
m	Middle
max	Maximum
n	nozzle
T	Total
the	Theoretical
0	State point at the inlet of the nozzle
1, 2	State points at the inlet and outlet of the rotating blade

Abbreviations

ARD	Average reaction degree
DAD	Dimensionless average diameter
DPST	Dual-pressure steam turbine
PO	Power output
SIA	Steam inlet angle
ST	Steam turbine

References

- Saito, E.; Matsuno, N.; Tanaka, K.; Nishimoto, S.; Yamamoto, R.; Imano, S. Latest technologies and future prospects for a new steam turbine. *Mitsubishi Heavy Ind. Tech. Rev.* **2015**, *52*, 39.
- Shibaev, T.L. A review of trends in development of cogeneration steam turbine units. *Thermal Eng.* **2020**, *67*, 903–908. [[CrossRef](#)]
- Chen, L.G.; Zhang, J.M.; Wu, C.; Sun, F.R. Analysis of multi-objective decision-making for marine steam turbine stage. *Int. J. Power Energy Syst.* **1998**, *18*, 96–101.
- Qin, X.Y.; Chen, L.G.; Sun, F.R.; Wu, C. Optimization for a steam turbine stage efficiency using a genetic algorithm. *Appl. Thermal Eng.* **2003**, *23*, 2307–2316. [[CrossRef](#)]
- Ni, H.; Xiao, H.; Zeng, F.M.; Sun, F.R. Segmented lumped parameter modeling of steam turbine based on cascade calculation. *J. System Simul.* **2014**, *26*, 294–299. (In Chinese)
- Abadi, S.M.A.N.R.; Ahmadvpour, A.; Abadi, S.M.N.R.; Meyer, J.P. CFD-based shape optimization of steam turbine blade cascade in transonic two phase flows. *Appl. Thermal Eng.* **2017**, *112*, 1575–1589. [[CrossRef](#)]
- Anđelić, N.; Mrzljak, V.; Lorencin, I.; Baressi Segota, S. Comparison of exergy and various energy analysis methods for a main marine steam turbine at different loads. *Pomor. Zb.* **2020**, *59*, 9–34. [[CrossRef](#)]
- Zhao, X.D.; Li, A.; Zhang, Y.J.; Ma, L.Q.; Ge, Z.H.; Du, X.Z. Performance improvement of low-pressure cylinder in high back pressure steam turbine for direct heating. *Appl. Thermal Eng.* **2021**, *182*, 116170. [[CrossRef](#)]
- Vedran, M.; Jasna, P.O.; Igor, P.; Ivica, G. Energy evaluation of a steam turbine from solar-based combined cycle power plant. *Mach. Tech. Mater.* **2022**, *16*, 86–89.
- Klonowicz, P.; Lampart, P.; Suchocki, T.; Zaniewski, D.; Klimaszewski, P. Optimization of an axial turbine for a small scale ORC waste heat recovery system. *Energy* **2020**, *205*, 118059.
- Klun, M.; Guzović, Z.; Rašković, P. Innovative small axial multistage turbine with partial admission for bottoming ORC. *Energy Rep.* **2021**, *7*, 9069–9093. [[CrossRef](#)]
- Symes, R.; Djaname, T.N.; Deligant, M.; Sauret, E. Design and optimization of a radial inflow turbine for use with a low temperature ORC. *Energies* **2021**, *14*, 8526. [[CrossRef](#)]
- Grönman, A.; Uusitalo, A. Analysis of radial-outflow turbine design for supercritical CO₂ and comparison to radial-inflow turbines. *Energy Convers. Mgmt.* **2022**, *252*, 115089. [[CrossRef](#)]
- Bejan, A. Street network theory of organization in nature. *J. Adv. Transp.* **1996**, *30*, 85–107. [[CrossRef](#)]
- Bejan, A. Constructal-theory network of conducting paths for cooling a heat generating volume. *Int. J. Heat Mass Transf.* **1997**, *40*, 799–816. [[CrossRef](#)]
- Bejan, A.; Lorente, S. *Design with Constructal Theory*; Wiley: Hoboken, NJ, USA, 2008.
- Chen, L.G. Progress in study on constructal theory and its applications. *Sci. China: Tech. Sci.* **2012**, *42*, 505–524. [[CrossRef](#)]

18. Chen, L.G.; Feng, H.J. *Multi-objective Constructal Optimization for Flow and Heat and Mass Transfer Processes*; Science Press: Beijing, China, 2017.
19. Chen, L.G.; Feng, H.J.; Xie, Z.H.; Sun, F.R. Progress of constructal theory in China over the past decade. *Int. J. Heat Mass Transf.* **2019**, *130*, 393–419. [[CrossRef](#)]
20. Chen, L.G.; Wu, W.H.; Feng, H.J. *Constructal Design for Heat Conduction*; Book Publisher International: London, UK, 2021.
21. Hajmohammadi, M.R.; Bahrami, M.; Ahmadian-Elmi, M. Thermal performance improvement of microchannel heat sinks by utilizing variable cross-section microchannels filled with porous media. *Int. Comm. Heat Mass Transf.* **2021**, *126*, 105360. [[CrossRef](#)]
22. Zhu, H.W.; Chen, L.G.; Ge, Y.L.; Feng, H.J. Constructal entropy generation rate minimization of heat conduction for leaf-shaped quadrilateral heat generation body. *Euro. Phys. J. Plus* **2022**, *137*, 275. [[CrossRef](#)]
23. Gungor, S.; Cetkin, E.; Lorente, S. Canopy-to-canopy liquid cooling for the thermal management of lithium-ion batteries, a constructal approach. *Int. J. Heat Mass Transf.* **2022**, *182*, 121918. [[CrossRef](#)]
24. Sun, K.; Feng, H.J.; Chen, L.G.; Ge, Y.L. Constructal design of a cooling channel with semi-circular sidewall ribs in a rectangular heat generation body. *Int. Comm. Heat Mass Transfer* **2022**, *134*, 106040. [[CrossRef](#)]
25. Bejan, A. *Heat Transfer: Evolution, Design and Performance*; Wiley: Hoboken, NJ, USA, 2022.
26. Bejan, A.; Gunes, U. Virus spreading and heat spreading. *Int. J. Thermal Sci.* **2022**, *174*, 107433. [[CrossRef](#)]
27. Xie, Z.J.; Feng, H.J.; Chen, L.G.; Wu, Z.X. Constructal design for supercharged boiler evaporator. *Int. J. Heat Mass Transf.* **2019**, *138*, 571–579. [[CrossRef](#)]
28. Feng, H.J.; Xie, Z.J.; Chen, L.G.; Wu, Z.X.; Xia, S.J. Constructal design for supercharged boiler superheater. *Energy* **2020**, *191*, 116484. [[CrossRef](#)]
29. Tang, W.; Feng, H.J.; Chen, L.G.; Xie, Z.J.; Shi, J.C. Constructal design for a boiler economizer. *Energy* **2021**, *223*, 120013. [[CrossRef](#)]
30. Guarino, F.; Cellura, M.; Traverso, M. Costructural law, exergy analysis and life cycle energy sustainability assessment: An expanded framework applied to a boiler. *Int. J. Life Cycle Assess.* **2020**, *25*, 2063–2085. [[CrossRef](#)]
31. Feng, H.J.; Chen, L.G.; Xie, Z.J.; Tang, W.; Ge, Y.L. Multi-objective constructal design for a marine boiler considering entropy generation rate and power consumption. *Energy Rep.* **2022**, *8*, 1519–1527. [[CrossRef](#)]
32. Nejad, A.H.; Ekici, K.; Sabau, A.S.; Bejan, A.; Arimilli, R.V. Counter cross-flow evaporator geometries for supercritical organic Rankine cycles. *Int. J. Heat Mass Transf.* **2019**, *135*, 425–435. [[CrossRef](#)]
33. Feng, H.J.; Chen, L.G.; Wu, Z.X.; Xie, Z.J. Constructal design of a shell-and-tube heat exchanger for organic fluid evaporation process. *Int. J. Heat Mass Transf.* **2019**, *131*, 750–756. [[CrossRef](#)]
34. Wu, Z.X.; Feng, H.J.; Chen, L.G.; Xie, Z.J.; Cai, C.G. Pumping power minimization of an evaporator in ocean thermal energy conversion system based on constructal theory. *Energy* **2019**, *181*, 974–984. [[CrossRef](#)]
35. Cai, C.G.; Feng, H.J.; Chen, L.G.; Wu, Z.X.; Xie, Z.J. Constructal design of a shell-and-tube evaporator with ammonia-water working fluid. *Int. J. Heat Mass Transf.* **2019**, *135*, 541–547. [[CrossRef](#)]
36. Bejan, A.; Lee, J.; Lorente, S.; Kim, Y. The evolutionary design of condensers. *J. Appl. Phys.* **2015**, *117*, 125101. [[CrossRef](#)]
37. Feng, H.J.; Cai, C.G.; Chen, L.G.; Wu, Z.X.; Lorenzini, G. Constructal design of a shell-and-tube condenser with ammonia-water working fluid. *Int. Comm. Heat Mass Transf.* **2020**, *118*, 104867. [[CrossRef](#)]
38. Wu, Z.X.; Feng, H.J.; Chen, L.G.; Ge, Y.L. Performance optimization of a condenser in OTECS based on constructal theory and multi-objective genetic algorithm. *Entropy* **2020**, *22*, 641. [[CrossRef](#)]
39. Feng, H.J.; Tang, W.; Chen, L.G.; Shi, J.C.; Wu, Z.X. Multi-objective constructal optimization for marine condensers. *Energies* **2021**, *14*, 5545. [[CrossRef](#)]
40. Bejan, A.; Lorente, S.; Kang, D.H. Constructal design of regenerators. *Int. J. Energy Res.* **2013**, *37*, 1509–1518. [[CrossRef](#)]
41. Hajabdollahi, H.; Dehaj, M.S. Rotary regenerator: Constructal thermoeconomic optimization. *J. Taiwan Inst. Chem. Eng.* **2020**, *113*, 231–240. [[CrossRef](#)]
42. Kim, Y.S.; Lorente, S.; Bejan, A. Distribution of size in steam turbine power plants. *Int. J. Energy Res.* **2009**, *33*, 989–998. [[CrossRef](#)]
43. Beyene, A.; Peffley, J. Constructal theory, adaptive motion, and their theoretical application to low-speed turbine design. *J. Energy Eng.* **2009**, *135*, 112–118. [[CrossRef](#)]
44. Feng, H.J.; Chen, L.G.; Xie, Z.H.; Sun, F.R. Constructal design for gas-turbine blade based on minimization of maximum thermal resistance. *Appl. Therm. Eng.* **2015**, *90*, 792–797. [[CrossRef](#)]
45. Stanescu, G.; Barbu, E.; Vilag, V.; Andreescu, T. Constructal approach on the feasibility of compressed air temperature control by evaporative cooling in gas turbine power plants. *Proc. Rom. Acad. Ser. A* **2018**, *19*, 201–206.
46. Wu, Z.X.; Feng, H.J.; Chen, L.G.; Xie, Z.J.; Cai, C.G.; Xia, S.J. Optimal design of dual-pressure turbine in OTEC system based on constructal theory. *Energy Convers. Manag.* **2019**, *201*, 112179. [[CrossRef](#)]
47. Chen, L.G.; Wu, Z.X.; Feng, H.J.; Ge, Y.L. Constructal design for dual-pressure axial-flow turbine in organic Rankine cycle. *Energy Rep.* **2022**, *8*, 45–55. [[CrossRef](#)]
48. Wu, Z.X.; Feng, H.J.; Chen, L.G.; Tang, W.; Shi, J.C.; Ge, Y.L. Constructal thermodynamic optimization for ocean thermal energy conversion system with dual-pressure organic Rankine cycle. *Energy Convers. Manag.* **2020**, *210*, 112727. [[CrossRef](#)]
49. Feng, H.J.; Wu, Z.X.; Chen, L.G.; Ge, Y.L. Constructal thermodynamic optimization for dual-pressure organic Rankine cycle in waste heat utilization system. *Energy Convers. Manag.* **2021**, *227*, 113585. [[CrossRef](#)]

-
50. Wu, Z.X.; Chen, L.G.; Feng, H.J.; Ge, Y.L. Constructal thermodynamic optimization for a novel Kalina-organic Rankine combined cycle to utilize waste heat. *Energy Rep.* **2021**, *7*, 6095–6106. [[CrossRef](#)]
 51. Xiao, Z.H.; Sheng, W. *Steam Turbine Equipment and System*; China Electric Power Press: Beijing, China, 2008. (In Chinese)